

Low-Loss High-Fidelity Frequency-Mode Hadamard Gates Based on Electromagnetically Induced Transparency

Kao-Fang Chang¹, Ta-Pang Wang¹, Chun-Yi Chen¹, Yi-Hsin Chen^{2,5},
Yu-Sheng Wang¹, Yong-Fan Chen^{3,5,*}, Ying-Cheng Chen^{4,5}, and Ite A. Yu^{1,5,*}

¹*Department of Physics, National Tsing Hua University, Hsinchu 30013, Taiwan*

²*Department of Physics, National Sun Yat-sen University, Kaohsiung 80424, Taiwan*

³*Department of Physics, National Cheng Kung University, Tainan 70101, Taiwan*

⁴*Institute of Atomic and Molecular Sciences, Academia Sinica, Taipei 10617, Taiwan*

⁵*Center for Quantum Technology, Hsinchu 30013, Taiwan*

(Dated: September 25, 2022)

Frequency-encoded photonic qubits are not only more stable over long transmission distances but also more robust against birefringent materials. A 50/50 frequency beam splitter (FBS) is the Hadamard gate in quantum logic operation, which coherently converts a photon in one frequency or wavelength mode to another photon in the superposition of two different modes. Previous works revealed that the Hadamard gates or FBS's operating at the single-photon level had overall efficiencies or output-to-input ratios less than 50%. Here, our FBS is made with the four-wave mixing (FWM) process based on the dual- Λ electromagnetically induced transparency (EIT) scheme. We achieved an overall efficiency of $90\pm 4\%$ with coherent-state single photons, which is the best up-to-date record for 50/50 FBS. In addition, we utilized this EIT-based scheme to perform wavelength conversion with light pulses of photon number less than one. We obtained an output-to-input ratio of $84\pm 4\%$, which is not only the highest record currently achieved, but also the first experimental demonstration of preservation of the quantum state in the dual- Λ EIT scheme. This demonstration was revealed by the fidelity of our Hadamard gate. To measure the fidelity, we propose a novel method using Hong-Ou-Mandel interference (HOMI) for quantum process tomography. The fidelity of our Hadamard gate indicated by the HOMI's $g^{(2)}$ measurement is 0.99 ± 0.01 . This low-loss high-fidelity Hadamard gate or wavelength converter based on the dual- Λ EIT scheme can lead to useful operations or devices, such as entanglement swapping, multiplexer, etc., in long-distance quantum communication.

Quantum information is fragile and cannot be duplicated or amplified. Since photons do not collide with each other and hardly interact with the environment, they are the ideal carriers for quantum information and can preserve carried information intact over appreciable distances. Quantum information or wave functions is commonly encoded in photons' polarization or spatial mode. As compared with these two kinds of photonic qubits, frequency-encoded qubits are not only more stable over long transmission distances but also more robust against birefringent materials, attracting great attention recently [1–6]. Quantum logic operation is a desirable add-on feature of photonic qubits [4]. Among quantum logic operations, the Hadamard gate is an essential component, and transforms state $|0\rangle$ (or $|1\rangle$) to the superposition state of $|0\rangle$ and $|1\rangle$ of equal amplitude (or its orthogonal state). A beam splitter or polarizing beam splitter is exactly the Hadamard gate for spatial-mode or polarization qubits. In the context of frequency-encoded qubits, a frequency beam splitter (FBS) is the Hadamard gate, which coherently converts a photon in one frequency or wavelength mode to another photon in the superposition of two different frequency modes. A low-loss and high-fidelity frequency-mode Hadamard gate is crucial to the development of optical quantum computation of

frequency-encoded qubits.

In this work, we demonstrate a FBS with tunable split ratio. A FBS with the split ratio of 0.5 or a 50/50 FBS can be employed as the frequency-mode Hadamard gate. A FBS with the split ratio of 1 can be utilized as the quantum frequency converter (QFC) in long-distance quantum communication. To date, all kinds of 50/50 FBS and QFC operating at the single-photon level had output-to-input ratios or overall efficiencies less than 50% [5–16]. Most of these works suffered large insertion loss induced by media, which not only reduces the output-to-input ratio but also may lead to additional quantum noise. Here, our low-loss FBS is made with the four-wave mixing (FWM) process based on the dual- Λ electromagnetically induced transparency (EIT) scheme [17–24]. This EIT-based FWM process provides high optical nonlinearity, while greatly suppressing the insertion loss. Using the transition scheme depicted in Fig. 1(a), we converted a coherent-state single photon in the 780 nm mode to another photon in the superposition of 780 nm and 795 nm modes, and demonstrated a 50/50 FBS with an output-to-input ratio of $90\pm 4\%$. Furthermore, we performed a QFC from 780 to 795 nm with light pulses of photon number less than one, and observed an output-to-input ratio of $84\pm 4\%$. Both output-to-input ratios are the best up-to-date records.

To test the fidelity of the photonic Hadamard gate, one should perform quantum process tomography [25–28]. We propose a novel method for quantum process to-

*yu@phys.nthu.edu.tw; yfchen@mail.ncku.edu.tw

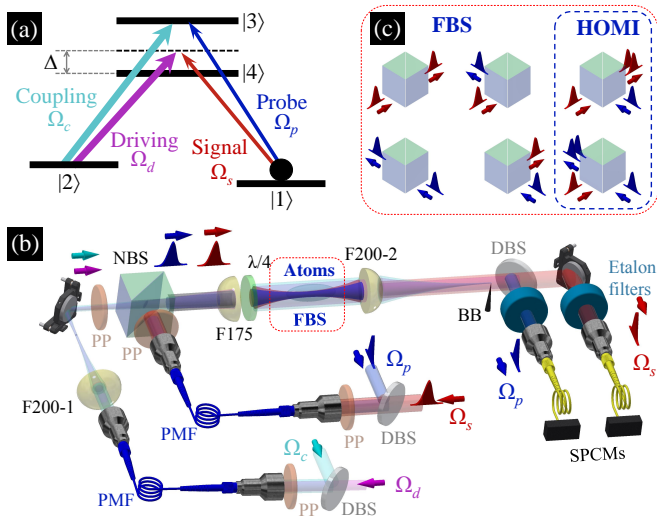


FIG. 1: Transition diagram, experimental setup, and operation of FBS. (a) Relevant energy levels and laser excitations in the experiment. $|1\rangle$, $|2\rangle$, $|3\rangle$, and $|4\rangle$ represent the states $|5S_{1/2}, F=1, m=1\rangle$, $|5S_{1/2}, F=2, m=1\rangle$, $|5P_{3/2}, F=2, m=2\rangle$, and $|5P_{1/2}, F=2, m=2\rangle$ of ^{87}Rb atoms, respectively. The coupling (Ω_c) and probe (Ω_p) fields with the wavelength of 780 nm drove the transitions resonantly. The driving (Ω_d) and signal (Ω_s) fields with the wavelength of 795 nm drove the transitions with a detuning of Δ . (b) Schema of the experimental setup. DBS: dichroic beam splitter; PP: polarizer or polarizing beam splitter with half-wave plate; PMF: polarization-maintained optical fiber; PBS: polarizing beam splitter; NBS: non-polarizing beam splitter with $T/R = 90/10$; F200-1, F175, F200-2: lenses with focal lengths of 200, 175, and 200 mm; $\lambda/4$: quarter-wave plate; BB: beam block; SPCM: single-photon counting module. (c) Illustration of 50/50 FBS. The left four diagrams depict that a 780 nm (or 795 nm) photon arriving to the input can result in either a 780 nm photon or a 795 nm photon with the equal probability at the output. The right two diagrams depict that a 780 nm and a 795 nm photons simultaneously arriving to the input can produce two photons of the same wavelength at the output due to the Hong-Ou-Mandel interference.

mography using Hong-Ou-Mandel interference (HOMI). [29–33]. The HOMI is a two-photon phenomenon, in which one two-mode wave function formed by two outputs of the Hadamard gate interferes with another. The value of normalized cross correlation function, $g^{(2)}$, in the HOMI measurement indicates that the fidelity of our Hadamard gate is 0.99 ± 0.01 . To our knowledge, this is the first time that the HOMI is used for quantum process tomography of a quantum logic gate. The high fidelity of our Hadamard gate also indicates that the single-photon quantum state is well preserved in the dual- Λ EIT scheme.

Our experiment was carried out with laser-cooled ^{87}Rb atoms [34–36]. Figure 1(b) shows the schema of experimental setup. In the photon-atom coupling scheme as depicted in Fig. 1(a), the 780 nm probe and coupling fields form the first EIT configuration under the one-photon

resonance; the 795 nm signal and driving fields form the second one with a large one-photon detuning, Δ . The coupling and driving fields were strong quasi-cw light. The probe and signal fields were weak classical pulses, or coherent-state single- or few-photon pulses. Other details of the experimental system can be found in Sec. I of the Supplemental Material.

To characterize our experimental system and verify measurement outcomes, we made theoretical predictions with the optical Bloch equations (OBEs) of density-matrix operator and the Maxwell-Schrödinger equations (MSEs) of light fields, which can be found in Sec. II of the Supplemental Material. In these equations and thorough the paper, Ω_c , Ω_d , Ω_p , and Ω_s denote the Rabi frequencies of the coupling, driving, probe, and signal fields, δ is the two-photon detuning of the Raman transition between two ground states $|1\rangle$ and $|2\rangle$, γ represents the ground-state decoherence rate, Γ denotes the spontaneous decay rate of the excited states $|3\rangle$ and $|4\rangle$ which is about $2\pi \times 6$ MHz in our case, and α is the optical depth (OD) of the medium. The measurements that determined Ω_c , Ω_d , γ , and α in the experiment are illustrated in Sec. III of the Supplemental Material.

The split ratio is defined as the ratio of 795 nm output energy to total output energy, which is actually the photon-number ratio through this work to account for the energy difference between 780 nm and 795 nm photons. Tuning the split ratio of FBS can be done by varying either two-photon detuning δ or one-photon detuning Δ . In this study of split ratio, only the 780 nm probe pulse of classical light was present at the input, and $\Omega_c = \Omega_d$. A part of the 780 nm input pulse was converted to the 795 nm signal pulse at the output, and the remaining became the 780 nm output pulse. Figures 2(a) and 2(b) show the energy transmissions of 780 nm and 795 nm output pulses as functions of the two-photon detuning δ and the one-photon detuning Δ , respectively. One can see that using δ to tune the split ratio can suffer a larger loss, and using Δ is more efficient. In Fig. 2(b), the split ratio can be tuned from 1 to 0.5 or smaller with $|\Delta|/(2\pi) \geq 130$ MHz. The total energy transmission of 780 nm and 795 nm output pulses is 85% (or 88%) at the split ratio equal to 0.97 (or 0.54). A smaller split ratio results in a higher total transmission. In both figures, the apparent phenomenon of oscillation indicates that the underlying mechanism of FWM involves with the interference effect [21, 22]. The theoretical predictions were calculated by numerically solving OBEs and MSEs with the experimentally-determined parameters of α , Ω_c , Ω_d , and γ [35, 36]. Consistency between the experimental data and theoretical predictions is satisfactory.

To test whether the scheme of our FBS can also work well at the single-photon level, we performed the measurements with coherent-state pulses of photon number equal to or less than 1. Two etalon filters were installed to provide the extinction ratio of 43 dB. The etalons, together with the scheme of spatial filter (see the third paragraph in Sec. I of the Supplemental Material), can ef-

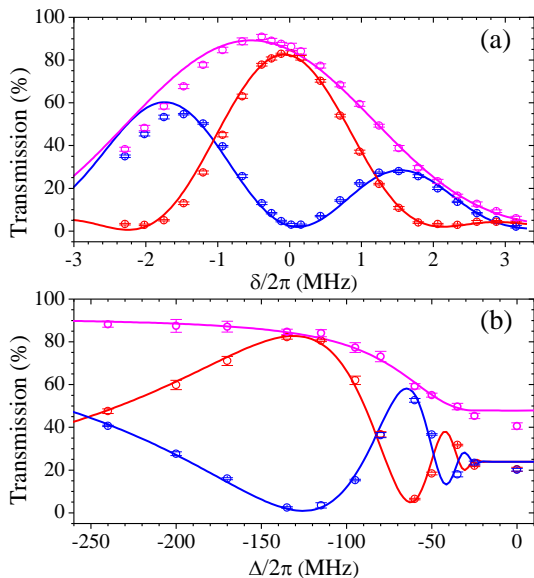


FIG. 2: Tuning the split ratio of frequency beam splitter. (a) At one-photon detuning $\Delta = -2\pi \times 135$ MHz, transmissions as functions of two-photon detuning δ , where $\delta = 0$ is defined by the maximum transmission of the output signal pulse, but not by making the two-photon Raman transition of $|1\rangle \rightarrow |2\rangle$ resonant. (b) At $\delta = 0$, transmissions as functions of $\Delta/(2\pi)$. In (a) and (b), only the 780 nm probe pulse with the e^{-2} full width of $3.0 \mu\text{s}$ was present at the input. Blue, red, and magenta circles are the experimental data of 780 nm probe and 795 nm signal output transmissions, and their total transmission, respectively. Solid lines are the theoretical predictions calculated with $\Omega_c = \Omega_d = 3.0\Gamma$, α (OD) = 130, and $\gamma = 3 \times 10^{-3}\Gamma$, which were experimentally determined by the method illustrated in Sec. III of the Supplemental Material. The asymmetry between positive and negative values of δ is due to the existence of a phase mismatch in the experimental system.

fectively block the strong coupling and driving light from entering single-photon counting modules (SPCMs). Two Excelitas SPCM-AQRH-13-FC were used to detect the 780 nm and 795 nm output photons. The collection efficiencies (including the SPCM's quantum efficiency) of the 780 nm and 795 nm photons were about 0.13 and 0.12 for the data in Fig. 3(a) [0.17 and 0.12 for those in Fig. 3(b)]. We had another SPCM at the input to monitor the input photon number. All of the photo multiplier tubes used in the measurements of classical-light pulses and the SPCMs used in those of single-photon or few-photon pulses were calibrated to account for different detection efficiencies between the wavelengths or between the detectors. In each SPCM's counting, it took 0.15 s to replenish cold atoms, switch off the MOT, perform the temporal dark-MOT, and optically pump all population to a single Zeeman state, before the input pulse was fired.

At the split ratio of 1, the FBS acts like a coherent wavelength converter transforming 780 nm photons completely into 795 nm photons. Figure 3(a) shows SPCM counts of input and output photons as functions of time.

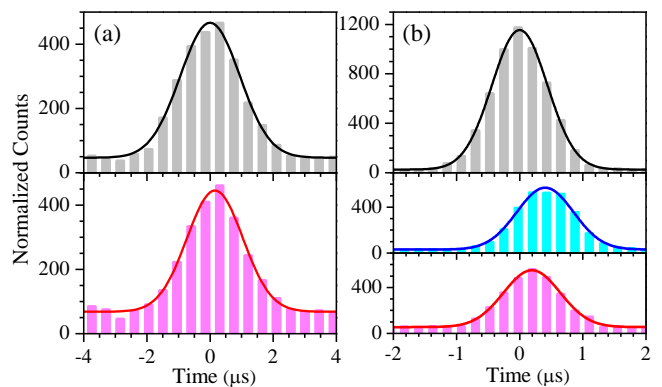


FIG. 3: Single-photon operations of frequency converter in (a) and frequency beam splitter in (b). In (a), the number of input photon per pulse was 0.68, and the split ratio is nearly 1 set by $\Delta/(2\pi) = -125$ MHz. Top: counts of 780 nm input photons; bottom: those of 795 nm output photons. In (b), the number of input photon per pulse was 1.0, and the split ratio was about 0.5 set by $\Delta/(2\pi) = -210$ MHz. Top: counts of 780 nm input photons; middle and bottom: those of 780 nm and 795 nm output photons. In (a) or (b), the width of time bin for SPCM counts was 450 ns or 225 ns, and the data were the results of 24,000 or 32,000 measurements. All of black, red, and blue lines are the Gaussian best fits. Excluding the baseline count, the ratios of output to input photon numbers are $84 \pm 4\%$ in (a) and $90 \pm 4\%$ in (b).

The best fit of the data in Fig. 3(a) is consistent with the result of classical light shown by Fig. S1(c) in Sec. III of the Supplemental Material. The baseline count was mainly contributed from the leakage of strong coupling or driving fields. Using the area below the best fit but excluding the baseline count, we determined the overall conversion efficiency from the 780 nm single photons to the 795 nm single photons or the output-to-input ratio is $84 \pm 4\%$.

The split ratio of 0.5 can make the 50/50 FBS or Hadamard gate for frequency-encoded photonic qubits. In Fig. 3(b), SPCM counts of 780 nm input photons and those of 780 nm and 795 nm output photons are plotted against time. The best fits of the data in Fig. 3(b) are consistent with the results of classical light shown by Fig. S2(a) in Sec. IV of the Supplemental Material. The comparison between Figs. 3(a) and 3(b) indicates that employing a narrower single-photon pulse can increase the amplitude-to-baseline ratio, while the output-to-input ratio was nearly intact. In our 50/50 FBS, the total transmission or ratio of total output photons to input photons is $90 \pm 4\%$.

We have now made the FBS which can operate with single photons. In analogy to an ordinary BS, 780 nm (or 795 nm) input photons are reflected into 795 nm (or 780 nm) output photons and transmitted into 780 nm (795 nm) output photons by our FWM-based FBS, with the split ratio defined by the ratio of reflected output photon number to total output photon number. Figure 1(c) illustrates the operation of 50/50 FBS. The next ques-

tion is whether this FBS can be suitable for quantum information processing. To answer the question, fidelity F is the important issue and can be determined by the following formula [6, 37, 38]:

$$F = \frac{|\text{Tr} [\hat{V}^\dagger \hat{U}]|^2}{4T}, \quad (1)$$

where \hat{U} represents the operator of an ideal BS, \hat{V} represents the operator of FWM-based FBS in the case here, $\text{Tr}[\dots]$ means the operation of trace, and T is the total transmission or success probability of \hat{V} .

Considering the FBS, we define t_1 (t_2) and r_1 (r_2) as the transmission and reflection coefficients of input 1 (input 2), and ϕ_1 (ϕ_2) as the phase difference between the reflected and transmitted outputs. The general expression of \hat{V} is given by

$$\begin{bmatrix} t_1 & r_2 e^{i\phi_2} \\ r_1 e^{i\phi_1} & t_2 \end{bmatrix}. \quad (2)$$

The split ratio of two inputs are determined by $r_1^2/(t_1^2 + r_1^2)$ and $r_2^2/(t_2^2 + r_2^2)$. In reality, the ground-state decoherence rate γ in the experimental system was not negligible, making two inputs produce different split ratios and $\phi_1 \neq \phi_2$. An ideal 50/50 BS must have $\phi_1 + \phi_2 = \pi$. Corresponding to \hat{V} in Eq. (2) of a realistic BS with two split ratios close to 0.5, \hat{U} of the ideal 50/50 BS can be written as [39, 40]

$$\hat{U} = \frac{1}{\sqrt{2}} \begin{bmatrix} 1 & e^{i(\pi-\Delta\phi)/2} \\ e^{i(\pi+\Delta\phi)/2} & 1 \end{bmatrix}, \quad (3)$$

where $\Delta\phi \equiv \phi_1 - \phi_2$. The derivation in Sec. V of the Supplemental Material shows that the fidelity of \hat{V} is

$$F = \frac{1}{2} + \frac{\bar{t}\bar{r}}{T} \sin\left(\frac{\phi}{2}\right), \quad (4)$$

where $\bar{t} = (t_1 + t_2)/2$, $\bar{r} = (r_1 + r_2)/2$, $T = \bar{t}^2 + \bar{r}^2$, and $\phi = \phi_1 + \phi_2$.

According to Eq. (4), one can immediately see that the phase ϕ approaching to π can make a high-fidelity FBS. To determine ϕ , we employed the Hong-Ou-Mandel interference (HOMI) [29–33], and measured the normalized cross correlation function, $g^{(2)}$, between two outputs of the FBS. A simple example, to explain why the HOMI measurement can determine ϕ of Eq. (4), is illustrated in Sec. VI of the Supplemental Material. In the HOMI, it is well known that, with a 50/50 BS in the ideal condition, two Fock-state single photons results in $g^{(2)} = 0$ [29, 30], and two phase-uncorrelated coherent-state single photons results in $g^{(2)} = 0.5$ [31–33]. Here, we sent two pulses to the two input ports of 50/50 FBS in the HOMI measurement. Each pulse consisted of a coherent-state single photon or few photons. The wavelength of one pulse was 780 nm and that of the other was 795 nm. Since the two pulses had the same mean photon number

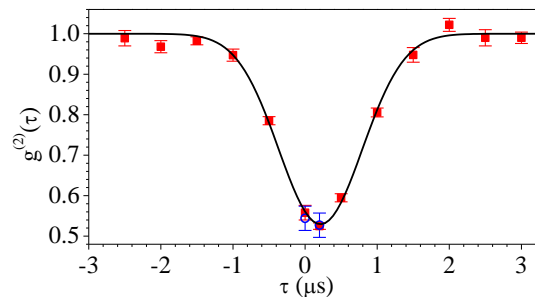


FIG. 4: Measurement of cross correlation function $g^{(2)}$ in the Hong-Ou-Mandel interference. $g^{(2)}$ is plotted against the delay time between two input pulses, τ . The experimental condition was very similar to that in Fig. S2 of the Supplemental Material. Blue circles are the experimental data taken at $\Delta/(2\pi) = -215$ MHz with two single-photon input pulses of 780 nm and 795 nm. Each circular data point, in which the contribution from background counts is removed, is the result of 28,800 measurements. Red squares are the experimental data taken at $\Delta/(2\pi) = -205$ MHz with two 5-photon input pulses. Each square data point, corrected for the saturation effect of SPCM's gain and the background contribution, is the result of 9,600 measurements. The two values of Δ , which set the split ratio of FBS to about 0.5, are different due to the day-to-day variation of OD. The e^{-2} full width of input pulses was $1.7 \mu\text{s}$. The time windows for SPCM counts of the blue circular and red square data points were 1.8 and $8.0 \mu\text{s}$, respectively. Solid line is the best fit of a Gaussian function with the e^{-2} full width of $2.3 \mu\text{s}$ and the minimum $g^{(2)}$ of 0.53.

and were phase-uncorrelated, the derivation in Sec. VII of the Supplemental Material shows that $g^{(2)}$ of the two output ports is given by

$$g^{(2)} = 1 + \frac{2t_1 t_2 r_1 r_2}{(t_1^2 + r_2^2)(t_2^2 + r_1^2)} \cos \phi. \quad (5)$$

In Fig. 4, $g^{(2)}$ is plotted against the delay time between the two input pulses. The minimum $g^{(2)}$ is 0.53 ± 0.03 and occurs at the delay time of 200 ns. Based on the data shown in Figs. S2(a) and S2(b) of the Supplemental Material, this 200-ns delay time is expected. The two-photon event of both photons from two input ports transmitting through the FBS, and that of both photons being reflected by the FBS were nearly indistinguishable under such delay time. Right before taking the data in Fig. 4, we measured the data similar to those in Figs. S2(a) and S2(b), and found $t_1^2 = 46\%$, $r_1^2 = 46\%$, $t_2^2 = 51\%$, and $r_2^2 = 39\%$. The minimum $g^{(2)}$ and Eq. (5) result in $\cos \phi = -0.94(6)$. Finally, we use Eq. (4) and the above values of t_1 , r_1 , t_2 , r_2 , and ϕ to determine $F = 0.99 \pm 0.01$, indicating that the FWM-based FBS possesses excellent fidelity.

In conclusion, utilizing the EIT-based FWM process we experimentally demonstrated a FBS of tunable split ratio with coherent-state single-photon pulses. At the split ratio of nearly 1, the FBS converted all of 780 nm input photons to 795 nm output photons with the

output-to-input ratio of $84\pm 4\%$, and can be employed as a quantum frequency converter. At the split ratio of 0.5, the FBS offered the output-to-input ratio of $90\pm 4\%$, and can be employed as the Hadamard gate for frequency-encoded photonic qubits. The overall efficiencies or output-to-input ratios of both frequency converter and 50/50 FBS are the best up-to-date records. To test the fidelity of the Hadamard gate, we proposed a method of the HOMI-type quantum process tomography, in which one two-mode wave function formed by two outputs of the Hadamard gate interferes with another. The measured value of $g^{(2)}$ indicates that the fidelity of the Hadamard gate is 0.99 ± 0.01 . To our knowledge, it is the first time to utilize the HOMI in the quantum process

tomography. This low-loss high-fidelity Hadamard gate or FBS can lead to a useful device for quantum operations in the long-distance quantum communication with frequency-encoded qubits, such as entanglement swapping, coherent frequency conversion, etc.

ACKNOWLEDGMENTS

This work was supported by the Ministry of Science and Technology of Taiwan under Grant Nos. 106-2119-M-007-003 and 107-2745-M-007-001.

-
- [1] A. Eckstein, B. Brecht, and C. Silberhorn, *A quantum pulse gate based on spectrally engineered sum frequency generation*, Opt. Express **19**, 13770 (2011).
- [2] B. Brecht, A. Eckstein, R. Ricken, V. Quijing, H. Suche, L. Sansoni, and C. Silberhorn, *Demonstration of coherent time-frequency Schmidt mode selection using dispersion-engineered frequency conversion*, Phys. Rev. A **90**, 030302(R) (2014).
- [3] M.-J. Lee, J. Ruseckas, C.-Y. Lee, V. Kudrišov, K.-F. Chang, H.-W. Cho, G. Juzeliūnas, and I. A. Yu, *Experimental demonstration of spinor slow light*, Nat. Commun. **5**, 5542 (2014).
- [4] J. M. Lukens and P. Lougovski, *Frequency-encoded photonic qubits for scalable quantum information processing*, Optica **4**, 8 (2017).
- [5] T. Kobayashi, R. Ikuta, S. Yasui, S. Miki, T. Yamashita, H. Terai, T. Yamamoto, M. Koashi, and N. Imoto, *Frequency-domain Hong-Ou-Mandel interference*, Nat. Photon. **10**, 441 (2016).
- [6] H.-H. Lu, J. M. Lukens, N. A. Peters, O. D. Odele, D. E. Leaird, A. M. Weiner, and P. Lougovski, *Electro-Optic Frequency Beam Splitters and Tritters for High-Fidelity Photonic Quantum Information Processing*, Phys. Rev. Lett. **120**, 030502 (2018).
- [7] L. M. Duan, M. D. Lukin, J. I. Cirac, and P. Zoller, *Long-distance quantum communication with atomic ensembles and linear optics*, Nature **414**, 413 (2001).
- [8] N. K. Langford, S. Ramelow, R. Prevedel, W. J. Munro, G. J. Milburn, and A. Zeilinger, *Efficient quantum computing using coherent photon conversion*, Nature **478**, 360 (2011).
- [9] P. Kumar, *Quantum frequency conversion*, Opt. Lett. **15**, 1476 (1990).
- [10] S. Tanzilli, W. Tittel, M. Halder, O. Alibart, P. Baldi, N. Gisin, and H. Zbinden, *A photonic quantum information interface*, Nature **437**, 116 (2005).
- [11] M. T. Rakher, L. Ma, O. Slattery, X. Tang, and K. Srinivasan, *Quantum transduction of telecommunications-band single photons from a quantum dot by frequency up-conversion*, Nat. Photon. **4**, 786 (2010).
- [12] H. J. McGuinness, M. G. Raymer, C. J. McKinstrie, and S. Radic, *Quantum Frequency Translation of Single-Photon States in a Photonic Crystal Fiber*, Phys. Rev. Lett. **105**, 093604 (2010).
- [13] S. Ates, I. Agha, A. Gulinatti, I. Rech, M. T. Rakher, A. Badolato, and K. Srinivasan, *Two-Photon Interference Using Background-Free Quantum Frequency Conversion of Single Photons Emitted by an InAs Quantum Dot*, Phys. Rev. Lett. **109**, 147405 (2012).
- [14] A. S. Clark, S. Shahnian, M. J. Collins, C. Xiong, and B. J. Eggleton, *High-efficiency frequency conversion in the single-photon regime*, Opt. Lett. **38**, 947 (2013).
- [15] Q. Li, M. Davanço, and K. Srinivasan, *Efficient and low-noise single-photon-level frequency conversion interfaces using silicon nanophotonics*, Nat. Photon. **10**, 406 (2016).
- [16] S. Clemmen, A. Farsi, S. Ramelow, and A. Gaeta, *Ramsey Interference with Single Photons*, Phys. Rev. Lett. **117**, 223601 (2016); A. Farsi, PhD thesis. Cornell University, 2015.
- [17] A. G. Radnaev, Y. O. Dudin, R. Zhao, H. H. Jen, S. D. Jenkins, A. Kuzmich, and T. A. B. Kennedy, *A quantum memory with telecom-wavelength conversion*, Nat. Phys. **6**, 894 (2010).
- [18] G. Wang, Y. Xue, J.-H. Wu, Z.-H. Kang, Y. Jiang, S.-S. Liu, and J.-Y. Gao, *Efficient frequency conversion induced by quantum constructive interference*, Opt. Lett. **35**, 3778 (2010).
- [19] Z.-Y. Liu, J.-T. Xiao, J.-K. Lin, J.-J. Wu, J.-Y. Juo, C.-Y. Cheng, and Y.-F. Chen, *High-efficiency backward four-wave mixing by quantum interference*, Sci. Rep. **7**, 15796 (2017).
- [20] M. Jain, H. Xia, G. Y. Yin, J. Merriam, and S. E. Harris, *Efficient Nonlinear Frequency Conversion with Maximal Atomic Coherence*, Phys. Rev. Lett. **77**, 4326 (1996).
- [21] M. G. Payne and L. Deng, *Consequences of induced transparency in a double- Λ scheme: Destructive interference in four-wave mixing*, Phys. Rev. A **65**, 063806 (2002).
- [22] C.-K. Chiu, Y.-H. Chen, Y.-C. Chen, I. A. Yu, Y.-C. Chen, and Y.-F. Chen, *Low-light-level four-wave mixing by quantum interference*, Phys. Rev. A **89**, 023839 (2014).
- [23] C.-Y. Lee, B.-H. Wu, G. Wang, Y.-F. Chen, Y.-C. Chen, and I. A. Yu, *High conversion efficiency in resonant four-wave mixing processes*, Opt. Express **24**, 1008 (2016).
- [24] M. Fleischhauer, A. Imamoglu, and J. Marangos, *Electromagnetically induced transparency: Optics in coherent media*, Rev. Mod. Phys. **77**, 633 (2005).
- [25] A. M. Childs, I. L. Chuang, and D. W. Leung, *Realization of quantum process tomography in NMR*, Phys. Rev. A

- 64**, 012314 (2001).
- [26] J. L. O'Brien, G. J. Pryde, A. Gilchrist, D. F. James, N. K. Langford, T. C. Ralph, and A. G. White, *Quantum process tomography of a controlled-NOT gate*, Phys. Rev. Lett. **93**, 080502 (2004).
- [27] R. C. Bialczak, M. Ansmann, M. Hofheinz, E. Lucero, M. Neeley, A. D. O'Connell, D. Sank, H. Wang, J. Wenner, M. Steffen, A. N. Cleland, and J. M. Martinis, *Quantum process tomography of a universal entangling gate implemented with Josephson phase qubits*, Nat. Phys. **6**, 409 (2010).
- [28] Y. Kim, Y.-S. Kim, S.-Y. Lee, S.-W. Han, S. Moon, Y.-H. Kim, and Y.-W. Cho, *Direct quantum process tomography via measuring sequential weak values of incompatible observables*, Nat. Commun. **9**, 192 (2018).
- [29] C. K. Hong, Z. Y. Ou, and L. Mandel, *Measurement of Subpicosecond Time Intervals between Two Photons by Interference*, Phys. Rev. Lett. **59**, 2044 (1987).
- [30] T. B. Pittman, D. V. Strekalov, A. Migdall, M. H. Rubin, A. V. Sergienko, and Y. H. Shih, *Can Two-Photon Interference be Considered the Interference of Two Photons?*, Phys. Rev. Lett. **77**, 1917 (1996).
- [31] J. G. Rarity, P. R. Tapster, and R. Loudon, *Non-classical interference between independent sources*, J. Opt. B: Quantum Semiclass. Opt. **7**, S171 (2005).
- [32] Y.-S. Kim, O. Slattery, P. S. Kuo, and X. Tang, *Conditions for two-photon interference with coherent pulses*, Phys. Rev. A **87**, 063843 (2013).
- [33] H. Chen, X.-B. An, J. Wu, Z.-Q. Yin, S. Wang, W. Chen, and Z.-F. Han, *Hong-Ou-Mandel interference with two independent weak coherent states*, Chin. Phys. B **25**, 020305 (2016).
- [34] Y.-W. Lin, H.-C. Chou, P. P. Dwivedi, Y.-C. Chen, and I. A. Yu, *Using a pair of rectangular coils in the MOT for the production of cold atom clouds with large optical density*, Opt. Express **16**, 3753 (2008).
- [35] Y.-H. Chen, M.-J. Lee, I.-C. Wang, S. Du, Y.-F. Chen, Y.-C. Chen, and I. A. Yu, *Coherent Optical Memory with High Storage Efficiency and Large Fractional Delay*, Phys. Rev. Lett. **110**, 083601 (2013).
- [36] Y.-H. Chen, M.-J. Lee, I.-C. Wang, and I. A. Yu, *Fidelity of electromagnetically-induced-transparency-based optical memory*, Phys. Rev. A **88**, 023805 (2013).
- [37] D. B. Uskov, L. Kaplan, A. M. Smith, S. D. Huver, and J. P. Dowling, *Maximal success probabilities of linear-optical quantum gates*, Phys. Rev. A **79**, 042326 (2009).
- [38] S. Rahimi-Keshari, M. A. Broome, R. Fickler, A. Fedrizzi, T. C. Ralph, and A. G. White, *Direct characterization of linear-optical networks*, Opt. Express **21**, 13450 (2013).
- [39] S. M. Barnett, J. Jeffers, and A. Gatti, *Quantum optics of lossy beam splitters*, Phys. Rev. A **57**, 2134 (1998).
- [40] R. Uppu, T. A. W. Wolterink, T. B. H. Trentup, and P. W. H. Pinkse, *Quantum optics of lossy asymmetric beam splitters*, Opt. Express **24**, 16440 (2016).